UDK 620.178.4:620.193:669.14
Original scientific article/Izvirni znanstveni članek

ISSN 1580-2949
MTAEC9, 55(5)681(2021)

STUDY ON ALTERNATE IMMERSION CORROSION BEHAVIOR AND MECHANISM OF SDCM DIE STEEL FOR HOT STAMPING

ŠTUDIJ IN MEHANIZEM POTOPNEGA KOROZIJSKEGA OBNAŠANJA ORODNEGA JEKLA VRSTE SDCM ZA VROČE ŠTANCANJE

Jiang Bin[1,2*], Zuo Pengpeng[1,2], Wu Xiaochun[1,2]

[1]College of Materials Science and Engineering, Shanghai University, Shanghai 200444, China
[2]State Key Laboratory of Advanced Special Steel, Shanghai University, Shanghai 200444, China

Prejem rokopisa – received: 2021-06-15; sprejem za objavo – accepted for publication: 2021-07-12

doi:10.17222/mit.2021.192

In this paper, an alternate immersion corrosion test of Cr-Mo-V series SDCM steel for hot stamping was carried out and different stresses were loaded with an in-house-made fixture. The results showed that, regardless of the hardness and stress, the corrosion mode of the material was uniform. Stress could significantly increase the corrosion rate, with a lower hardness and higher corrosion rate. Because of the existence of a corrosion removal layer (CRL), the maximum corrosion-pit depth could be reduced. The maximum corrosion-pit depth and corrosion-pit density (CPD, ρ_v) were used to describe the degree of corrosion damage. From low to high hardness, the CPD ρ_v and corrosion resistance increased gradually. With the increased tempering temperature, the hardness decreased, and the percentage of the carbide area in the field of view increased from 16.36 % to 24.32 %. Irregular spherical carbide $M_{23}(C, N)_6$, rich in Cr coarsened and consumed the Cr element in the material, which led to a decrease in the corrosion resistance. Through the polarization curve of dynamic potential, we found that the current density was increased with decreased hardness, from 28.53 μA/mm^2 to 40.93 μA/mm^2.

Keywords: stress corrosion, hardness, corrosion rate, hot stamping die steel

Povzetek: V članku je opisan izmenični potopni korozijski test Cr-Mo-V jekla vrste SDCM, namenjenega za vroče štancanje. Avtorji so izvajali teste pri različnih predobremenitvah jekla na doma izdelani napravi za obremenjevanje. Rezultati raziskave so pokazali, da je, ne glede na trdoto jekla in napetost, potek korozije materiala enak in enovit. Napetost lahko pomembno poveča hitrost korozije pri nižji trdoti jekla. Zaradi odstranjene izvorne korozijske plasti (CRL; angl.: Corrosion Removal Layer), se je zmanjšala maksimalna globina korozije. Za opis stopnje korozijskih poškodb, je bila uporabljena globina maksimalne korozijske jamice in gostota korozijskih jamic (CPD, ρ_v). Z naraščanjem trdote jekla, je CPD, ρ_v in odpornost proti koroziji postopno naraščala. Z naraščajočo temperaturo popuščanja jekla, se je trdota jekla postopoma zmanjševala in delež karbidov je narastel s 16,36 % na 24,32 %. Karbidi nepravilne krogličnе oblike $M_{23}(C, N)_6$, bogati na Cr, so rastli in uporabljali Cr iz matrice, kar je privedlo do zmanjševanja korozijske odpornosti. S pomočjo polarizacijskih krivulj dinamičnega potenciala, so avtorji ugotovili, da je z zmanjševanjem trdote jekla tokovna gostota naraščala od 28,53 μA/mm^2 do 40,93 μA/mm^2.

Ključne besede: napetostna korozija, trdota, hitrost korozije, jeklo za vroče štancanje

1 INTRODUCTION

Cr-Mo-V series die steel is widely used in the field of hot stamping. The hot stamping die steel mainly includes Cr7V, H13, HTCS–130, DIEVAR and SDCM.[1] The service environment of a hot stamping die is bad, and the hot stamping parts are quenched in the die. Therefore, a large number of cooling channels are distributed below the cavity surface. Die cracking, leading to water leakage is one of the main forms of die failure, which is usually related to the corrosion of the die cooling channel. The research on the water channel corrosion focuses on a closed cooling system such as pipeline steel[2–4] and nuclear power plant.[5–7] When the pitting corrosion is the most serious, it is easy to cause water leakage. Cyclic loading shortens the crack initiation life.

Full immersion corrosion is usually related to the surface roughness, stress, corrosion medium, temperature, etc. In addition, alternate immersion corrosion is also related to the water film thickness,[8–10] that is, when the humidity is high, the water film thickness on the surface of a sample is thicker, reducing the corrosion rate, while a thin film accelerates corrosion, and the water film thickness is related to the immersion time and humidity. Stress has an important influence on corrosion, mainly in two respects. On the one hand, the metal is subject to external force, which makes the surface passivation film or oxide film break, exposing fresh metal, which leads to corrosion of the broken place. On the other hand, under the action of external force, atoms deform sequentially, lattice defects increase and atomic activation energy increases, causing corrosion of the metal surface.[11–14]

In addition to the environment, stress and other factors, the microstructure of a material also has an important influence on corrosion.[15] For the same martensite structure, some scholars reported some achievements in this respect. For example, in martensitic stainless steel,[16] the martensite structure with a small amount of carbide

*Corresponding author's e-mail:
binjiang@shu.edu.cn (Jiang Bin)

formed after quenching is more corrosion-resistant than the structure with a large amount of carbide formed after quenching and tempering. This is mainly related to local Cr depletion. For Cr-Mo-6V alloy steel, the content of Cr is not high, usually between 1 *w*/% and 7 *w*/%. There are a lot of dispersed carbides in the martensite structure or boundary of a quenched and tempered structure,[17–19] and the corrosion resistance increases with the increase in the Cr content.[20,21] By tempering at a higher temperature, the hardness of the material is lower due to the coarsening of carbides.[22,23] Such carbide dispersion does not contribute significantly to the material strength due to a loss of coherency of carbide precipitates with the matrix, and this causes the depletion of Cr, Mo and V from the matrix during tempering.[24,25] These coarser carbides consume the Cr in the matrix material, resulting in reduced corrosion resistance. Alves et al.[26] suggested that the beneficial effect of Cr towards corrosion resistance of steel must rely on Cr being present as a substitutional solute in the matrix, not being žtied up' as a carbide precipitate.

At present, there is little research on the corrosion behavior of hot work die steel that has not attracted attention. However, die failure caused by water channel corrosion is becoming more and more important. After the formation of corrosion pits, due to the anodic dissolution reaction inside the pits, the corrosion pits grow up. Under the action of stress, a stress or strain concentration occurs in the corrosion pits. It is necessary to carry out a detailed study on crack initiation due to the interaction with corrosive environment.[15] The popular methods to study corrosion behavior are statistical methods. With a statistical analysis, we can study the main factors such as the size of corrosion pits and weightlessness. The generalized lambda distribution methods are used to fit the experimental depth distribution frequency, and extreme value statistic methods are used to study the depth distribution of the maximum corrosion pit.[27–29] In this paper, based on the above research methods, combined with the experimental factors, the factors of stress and hardness are introduced, the morphology is measured with a 3D optical profilometer, and a statistical analysis of the pitting size data is carried out to quantitatively study the influence of stress and hardness on alternate immersion corrosion damage. In order to explain the corrosion properties of materials with different hardness values, dynamic potential polarization curves are measured. In order to explain the corrosion behavior of a material with a different hardness, the corrosion pit density parameter (ρ_v) is introduced to more accurately indicate the corrosion pit, in this case, for a fully corroded surface. In addition to the corrosion rate, the maximum corrosion pit depth is also used to assess corrosion damage, which is affected by the corrosion pit density, ρ_v.

2 EXPERIMENTAL PART

2.1 Experimental material

The experimental material was Cr-Mo-V series die steel; the brand was SDCM, which was independently researched and developed by the Shanghai University.[30] This kind of steel has been widely used for hot stamping dies. The chemical composition of the material in *w*/% is 0.46 C, 0.42 Si, 0.66 Mn, 2.56 Cr, 2.35 Mo and 0.82 V. The billet was remelted with ESR and the samples were cut from a high-quality billet module. The heat treatment and hardness of the samples after the treatment are shown in **Table 1**.

Table 1: Hardness of the material after different heat-treatment processes

NO.	Quenching temperature /°C	First tempering /°C	Second tempering /°C	Hardness /HRC
1-1	1030 ± 5	570 ± 3	570 ± 3	54 ± 1
1-2	1030 ± 5	580 ± 3	580 ± 3	52 ± 1
1-3	1030 ± 5	595 ± 3	595 ± 3	50 ± 1

The tempering process had two times of tempering, each time for 2 h. The samples were ground and polished. The surface roughness R_a was 0.011–0.05 μm in order to minimize the influence of the surface state on corrosion. The surface was smooth and flat, and the sample size was (32 × 4 × 1) mm. The samples and fixture are shown in **Figure 1**. According to the national standard "Corrosion of metals and alloys – Stress corrosion testing – Part 2: Preparation and use of bent-beam speci-

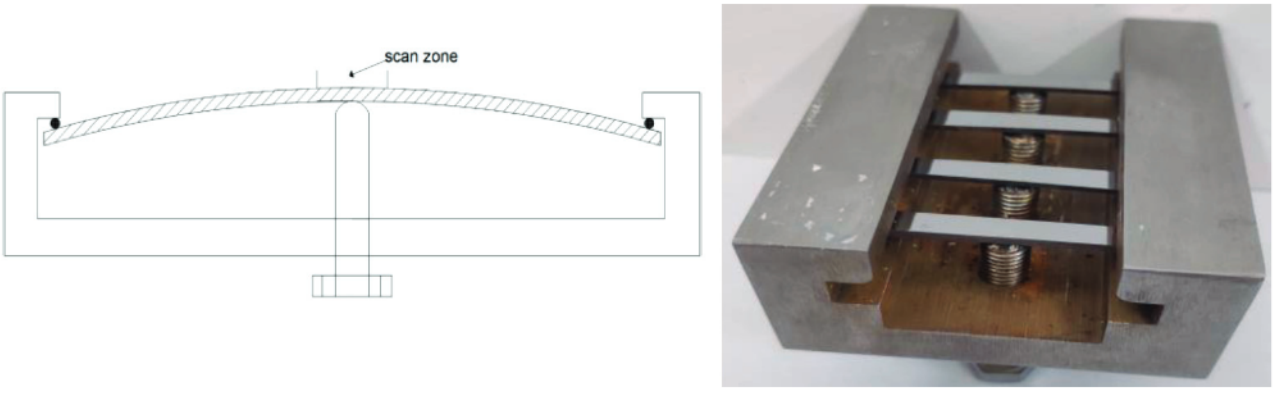

Figure 1: Three-point-bending loading and picture of the specimens

mens" (GB/T 15970.2–2000),[31] the stress at the convex point of a three-point-bending specimen was calculated. The convex point length of the specimen was 10 mm; it was the observation part during the corrosion experiment, while the rest was coated with silicone.

2.2 Experimental conditions and procedure

The corrosion test was carried out using the periodic infiltration method. The equipment model was YF–C1, as shown in **Figure 2**. The experimental procedure included soaking in deionized water for 10 min; the solution temperature was 25 ± 2 °C; then the samples were taken out for drying. Drying conditions included a relative humidity (RH) of not more than 45 % and a temperature of 30 ± 2 °C for 50 min. Before the experiment, the samples were weighed and taken out according to time points of (2, 5 and 24) h to observe their corrosion morphology. When the samples were taken out midway, they were only washed with deionized water without removing the corrosion products. After the observation, they were put back into the fixture to continue the experiment. After the experiment, corrosion products were removed and weighed, then the corrosion morphology was observed.

Three kinds of hardness materials were used for the test, the hardness values were (50 ± 1) HRC, (52 ± 1) HRC and (54 ± 1) HRC, hereinafter referred to as low hardness, medium hardness, high hardness, respectively. The hardness was tested with an HD9–45 type surface Rockwell hardness tester, the total test force was 1471 N (150 kg), the pressure dwell time was 6 s.

Figure 2: Alternate immersion corrosion equipment

The corrosion morphology was observed with a VHX-600 ultra-depth-of-field three-dimensional morphology microscope and Zeiss Supra 40 field-emission high-resolution scanning electron microscope (SEM). A Sensofar S neox 3D optical profilometer with a display resolution to 1 nm in the vertical direction and 120 nm in the horizontal direction was used to obtain the three-dimensional topography data of the sample surface. The JMatPro 7.0 software simulated the carbides sizes, and the Image-Pro Plus software calculated the area proportion of carbides.

In order to further explain different corrosion behaviors of the materials with different hardness values, polarization curves of high-, medium- and low-hardness materials were measured with a Gamry Framework Reference 600 potentiostat in a (35 ± 1) g/L neutral NaCl solution at 25 °C.

3 RESULTS

3.1 Corrosion morphology

The corrosion morphology of the samples with the hardness of 50 HRC quenched at 1030 °C and under different loading stresses is shown in **Figure 3**. The corrosion morphology of the samples without stress is shown in **Figure 3a**. The corrosion morphologies at the applied stress of (50, 100, 300 and 700) MPa are shown in **Figures 3b** to **3e**, respectively. After the stress is applied, the surface corrosion morphology is obviously different from that without the stress. The golden yellow rust on the surface disappears quickly and is replaced by gray black products. After 5 h, the golden yellow rust mostly disappeared; and it was replaced by gray black products after 24 h. The corrosion products are loose on the surface of the sample, and there is delamination. When the stress is not applied, corrosion pits can be seen. After the stress is applied, the corrosion pits are completely covered by rust.

For the samples with the hardness of 52 HRC quenched at 1030 °C, under different loading stresses, the corrosion morphology is shown in **Figure 4**, and the sample without the stress is shown in **Figure 4a**. The corrosion is more uniform, and the corrosion morphology is similar to that in **Figure 3a**. After the stress is applied, the corrosion morphology is similar to that of the 50 HRC samples. After 24 h, the area of golden rust on the surface is slightly larger than that in **Figure 3**.

For the specimens with the hardness of 54 HRC quenched at 1030 °C, under different loading stresses, the corrosion morphology is shown in **Figure 5**, and the no-stress specimen is shown in **Figure 5a**. The corrosion is more uniform, and the corrosion morphology is similar to those from **Figures 3a** and **4a**, but there is a slight corrosion in a local area, as shown with the red circles in the figures. After the stress was applied, the fading time of golden yellow rust on the surface was longer than for the above two kinds of samples. After 5 h, the stress was

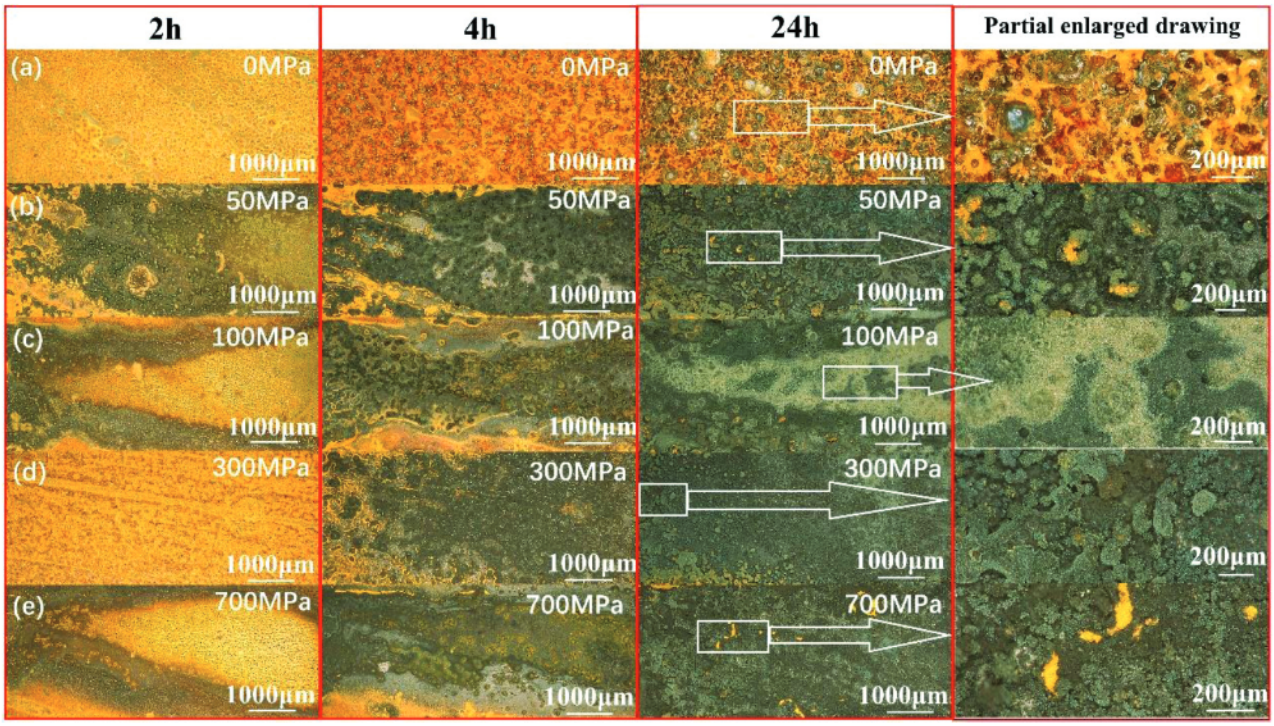

Figure 3: Corrosion morphology of specimens with hardness of 50 HRC (different stresses)

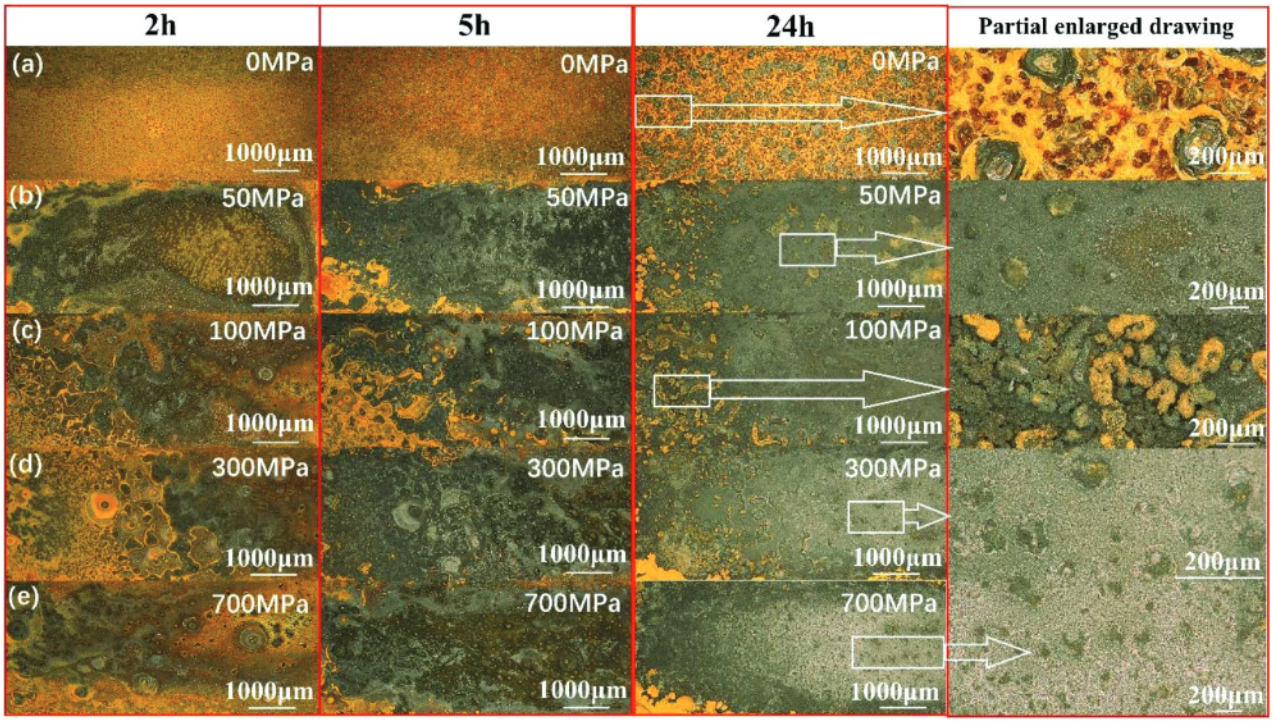

Figure 4: Corrosion morphology of specimens with hardness of 52 HRC (different stresses)

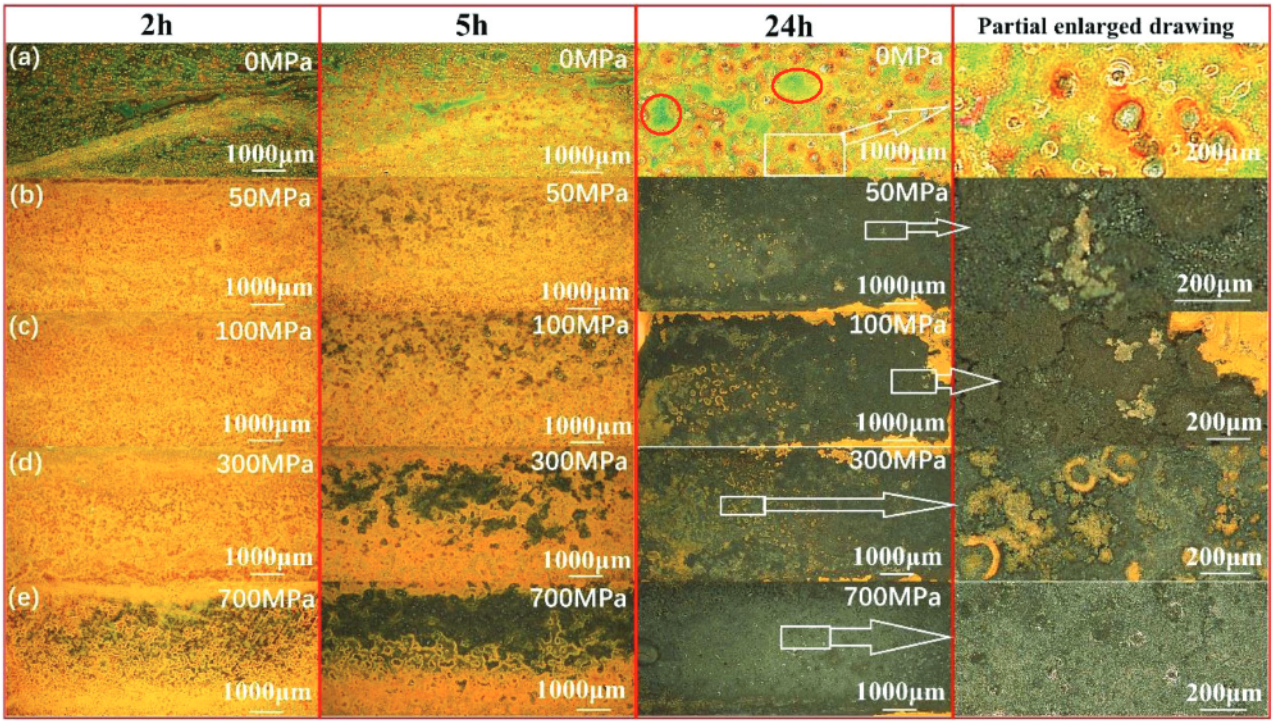

Figure 5: Corrosion morphology of specimens with hardness of 54 HRC (different stresses)

from 50–700 MPa, and the coverage of the golden yellow rust gradually decreased. After 24 h, there were still some residual areas, loose corrosion and delamination on the surface.

3.2 Corrosion-damage kinetics

The weight loss method is widely used to determine corrosion kinetics. However, due to different depths of a large number of corrosion pits, the use of only this method leads to an underestimation of corrosion damage. A 3D optical profilometer is used to reconstruct the surface topography, calculate the corrosion pit area, depth and other data and evaluate the corrosion damage by fitting the depth distribution. However, in uniform corrosion, a large number of corrosion pits are distributed and there are connected corrosion pits, so the number and depths of corrosion pits cannot be accurately counted. The uniform-corrosion process can be simply divided into two steps. The first step is shown in **Figure 6a**. When corrosion starts, small corrosion pits appear on the surface. As the corrosion progresses, a large number of corrosion pits form. The second step is shown in **Figure 6b** where a large number of corrosion products cover the metal surface, and the outermost layer is relatively

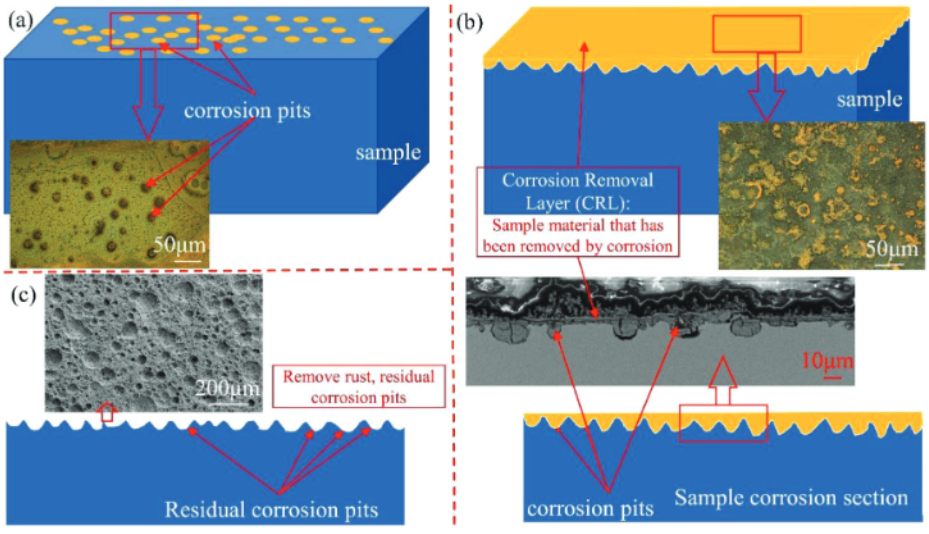

Figure 6: Uniform-corrosion diagram

loose. Through the corrosion section in the figure, it can be seen that the surface corrosion structure is composed of a corrosion removal layer (CRL) and corrosion pits. The CRL on the surface is entirely composed of rust of about 10 μm, while the corrosion pits are full of corrosion products. In order to describe the corroded surface more vividly, the corrosion products are chemically removed. As shown in **Figure 6c**, there is a large number of residual corrosion pits on the surface. Because of the existence of the CRL, the degree of corrosion damage cannot be accurately described directly, using the information of the corrosion pit morphology and size from **Figure 6c**; so, another parameter, the corrosion pit density, is defined.

Therefore, three indexes are used to evaluate the corrosion damage. One is the corrosion rate r_{corr}, which is calculated with the weight-loss method, the second is the introduced index of the corrosion pit density, and the third is the maximum corrosion pit depth.

Corrosion rate (r_{corr}):[32]

$$r_{corr} = \frac{\Delta m}{A\rho t} \tag{1}$$

Here, r_{corr} – corrosion rate (μm/h); Δm – weight loss (g); A – sample area (μm^2); ρ – density (g/cm^3); t – exposure time (h).

Total volume of corrosion loss:

$$V_{all} = V_{los} + V_{pits} \tag{2}$$

Here, V_{all} – volume converted by the total weight loss (μm^3); V_{los} – total volume of the surface layer removed by corrosion, the volume of the orange part in **Figure 6** (μm^3); V_{pits} – volume of the corrosion pits remaining on the surface of the specimen (μm^3), which can be obtained with a 3D optical profilometer

Definition of the corrosion pit density, ρ_v:

$$\rho_v = \frac{V_{pits}}{V_{all}} \tag{3}$$

ρ_v can better characterize corrosion damage, using the surface-corrosion morphology; generally speaking, $0 < \rho_v < 1$ when $\rho_v = 1$, which means that there is local corrosion on the surface, and the surface layer has not been corrosion removed. The larger the ρ_v value, the higher is the local corrosion tendency. The smaller the ρ_v value, the more the corrosion tends to be uniform. Under the same corrosion system, the ρ_v value can react to the degree of corrosion damage.

The effect of stress and hardness on the corrosion rate is shown in **Figure 7a**. Regardless of the hardness, the corrosion rate r_{corr} increases with an increase in the stress, but the increase rate is different. The corrosion rate of low-hardness materials seems to be more sensitive to stress. **Figure 7b** shows the increase percentage for the corrosion rate under different stresses relative to a corrosion rate of 0 MPa. It can be seen that the corrosion rate of low-hardness materials increases more rapidly at 50 MPa, and the increase rate is more than twice that of high-hardness materials. With a further increase in the stress, the corrosion rate of three kinds of hardness materials increases correspondingly, but the growth rate of high-hardness materials slows down, indicating that high-hardness materials are easier to resist stress corrosion. Although the total corrosion rate of low-hardness materials is higher, the corrosion rate of medium-hardness materials increases faster than that of low-hardness materials when the stress exceeds 100 MPa, which is mainly due to the high initial corrosion rate of low-hardness materials. As the stress increases, the corrosion-rate growth rate is not as fast as that of medium-hardness materials, and the corrosion resistance of high-hardness materials is the best among these three types of materials.

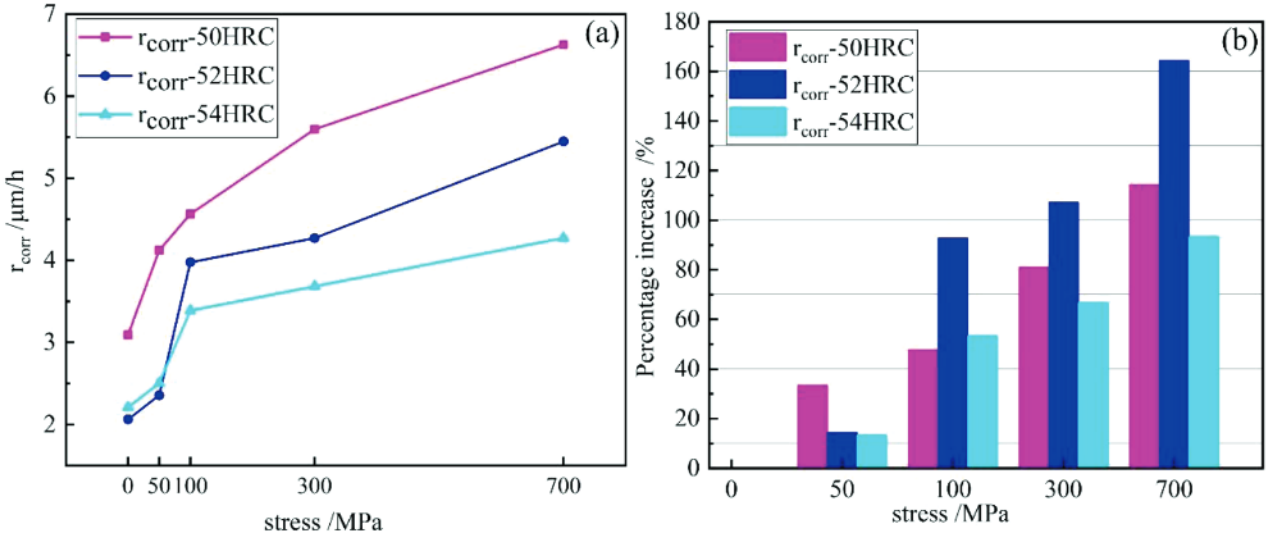

Figure 7: Influence curves of stress and hardness affecting corrosion rate: a) corrosion-rate curve, b) percentage increase in corrosion rate relative to no applied stress

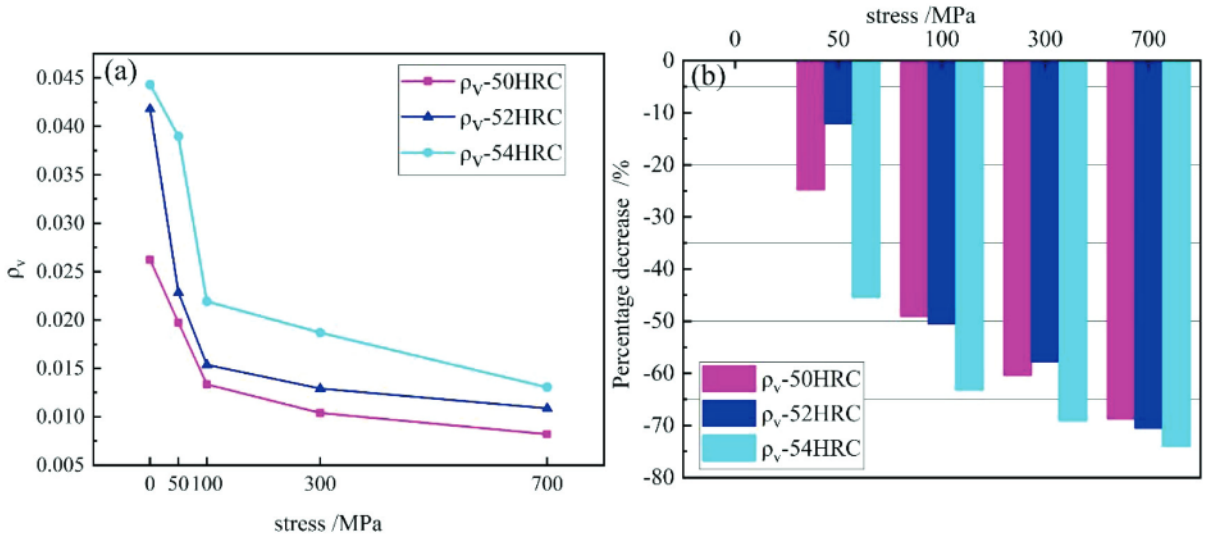

Figure 8: Influence curves of stress and hardness affecting corrosion-pit density: a) corrosion pit density curve, b) percentage decrease in corrosion pit density relative to no applied stress

Therefore, the corrosion-rate growth rate of medium-hardness materials is the highest.

Figure 8a shows curves of the corrosion pit density, ρ_v, with the change in the stress. In contrast to **Figure 7a**, regardless of the hardness, the corrosion pit density decreases with an increase in the stress, indicating that the volume of corrosion pits remaining on the corrosion surface decreases with the increase in the stress. This further indicates that in the comprehensive corrosion process, stress promotes corrosion, reducing the change in the corrosion-pit size. **Figure 8b** shows the percentage reduction of ρ_v under different stresses relative to the ρ_v of 0 MPa. It can be seen that, regardless of the hardness, after more than 100 MPa, although the reduction rate of ρ_v is higher, it decreases with the increase in the stress, while the reduction rate of ρ_v for high-hardness materials is always higher. This shows that with the increase in the stress, the volume of corrosion pits remaining on the corrosion surface decreases. In comparison with low-hardness materials, high-hardness materials are more corrosion resistant.

3.3 Maximum corrosion-pit depth

The above corrosion rate r_{corr} and CPD ρ_v describe the degree of corrosion, but the damage of the subsequent corrosion has not been accurately described. Generally speaking, the maximum corrosion-pit depth is an important index of stress corrosion. In this section, surface corrosion is detected with a 3D optical profiler, and the data of the maximum corrosion-pit depth S_V of surface corrosion is analyzed.

As shown in **Figure 9**, the maximum corrosion-pit depth does not always increase with the increase in the stress for the three types of hardness materials. For the low-hardness materials, the maximum corrosion-pit depth is not always obtained at the maximum stress of 700 MPa; the maximum corrosion-pit depth is 153.63 μm at 100 MPa. For high- and medium-hardness materials, the maximum corrosion-pit depth is 114.41 μm and 227.12 μm at 700 MPa, respectively. It can be seen from the figure that under different loading stresses, the maximum corrosion-pit depth is not the deepest at low hardness; it is the deepest at medium hardness and the shallowest at high hardness. For low- and medium-hardness materials, the maximum corrosion-pit depth decreases when the stress is 300 MPa, which is mainly due to the corrosion rate r_{corr} being higher at this stress compared with that at 100 MPa, especially at low hardness, while the corrosion rate increases by 22.58 % (calculated in **Figure 7a**). On the other hand, CPD ρ_v decreases slowly, resulting in a larger CRL of low-hardness materials, reducing the maximum corrosion-pit depth. This is also the reason why

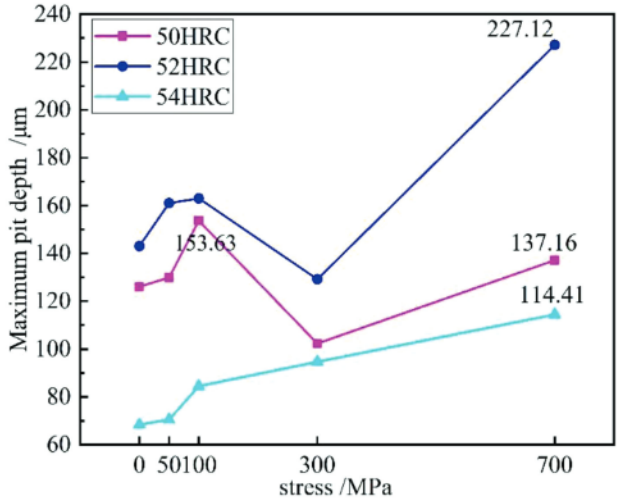

Figure 9: Influence curves of stress and hardness affecting the maximum corrosion-pit depth

the maximum corrosion-pit-depth curve for low-hardness materials is in the middle of **Figure 9**.

4 DISCUSSION

4.1 Effect of the stress on the maximum corrosion-pit depth

A power function is widely used to describe the dependence of the pit depth on the time and can be expressed as follows:[2,33,34]

$$x = \alpha t^{\beta} \tag{4}$$

The x and t values are the pit depth (m) and exposure time (h), respectively.

As this experiment is carried out over a certain period, and stress is the variable, we use stress (F) instead of t in Equation (4), and introduce constant K to express the thickness change in the CRL, as shown in Equation (5).

$$x = \alpha F^{\beta} + K \tag{5}$$

For high-hardness materials, the CRL in the corrosion process is smaller. Fitting Equation (6) is obtained:

$$x = 18.16F^{0.24} + K \qquad R^2 = 0.9756. \tag{6}$$

For low- and medium-hardness materials, the CRL is larger than for high-hardness materials in the corrosion process. While corrosion pits develop their depth, the surface is also corroded rapidly. Therefore, while increasing the corrosion rate, the stress cannot always increase the maximum corrosion-pit depth. The relationship between the pit depth and stress can be well fitted using a third-order polynomial, as shown in Equation (7):

$$x = k + aF + bF^2 + cF^3 \tag{7}$$

For low-hardness materials, the fitting Equation (8) is as follows

$$x = 122.2 + 0.49F + 0.0027F^2 + 2.94F^3 \qquad R^2 = 0.8797. \tag{8}$$

For medium-hardness materials, the fitting Equation (9) is as follows:

$$x = 143.8 + 0.42F + 0.0024F^2 + 2.82F^3 \qquad R^2 = 0.9989. \tag{9}$$

The fitting curves for the three kinds of hardness materials are shown in **Figure 10**. For high-hardness materials, the maximum corrosion-pit depth and stress are in the exponential form. At the initial stress of 100 MPa, the maximum corrosion-pit depth increases rapidly with the increase in the stress. At 100 MPa, the maximum corrosion-pit depth increases slowly with the increase in the stress. For medium- and low-hardness materials, the relationship between the maximum corrosion-pit depth and stress is in the form of an "S" curve. Especially for low-hardness materials, stress has a great impact on the corrosion rate; with a larger CRL, ρ_v decreases, and the stress is not sensitive to the maximum corrosion-pit depth. For medium-hardness materials, the maximum corrosion-pit depth increases significantly under high stress (about 700 MPa), but it is not sensitive to low stress. However, on the whole, the maximum corrosion-pit depth is the deepest in this case. According to the fitting curve, even at the lowest point of the "S"

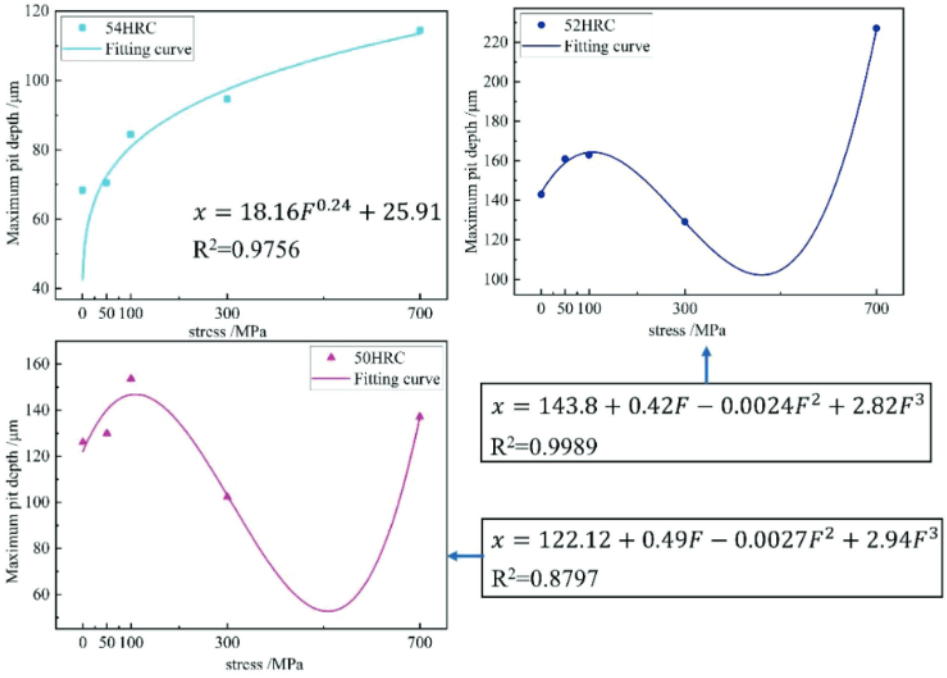

Figure 10: Fitting curves of stress to maximum corrosion-pit depth

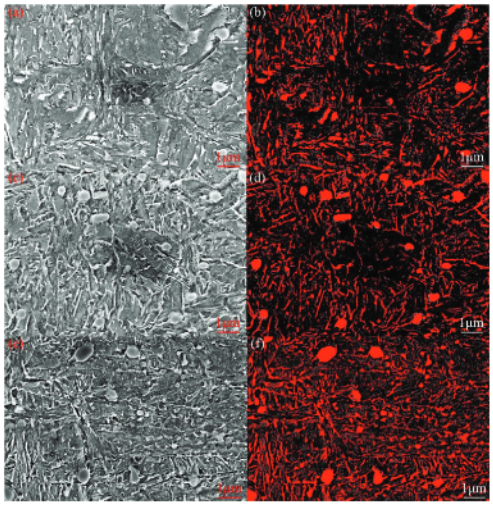

Figure 11: Different SEM hardness photos and carbide renders: a), c), e): SEM photos for hardness values of (54, 52, 50) HRC, respectively, b), d), f): carbide renders for hardness values of (54, 52, 50) HRC, respectively

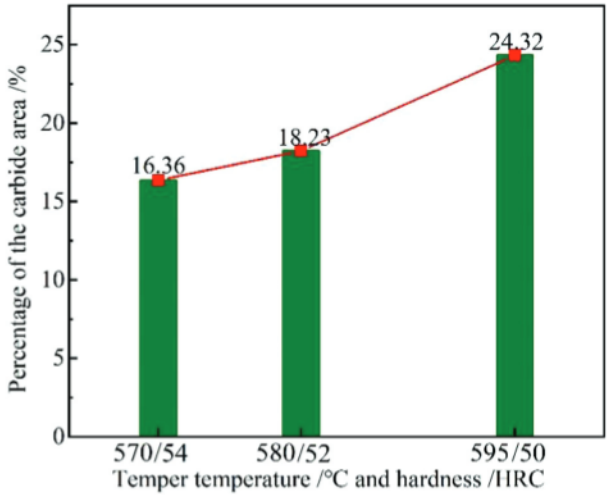

Figure 12: Calculation of carbide area and percentage of field by Image-Pro Plus software

curve, the maximum corrosion-pit depth is more than 100 μm.

4.2 Effect of the hardness and microstructure on corrosion

It is well known that the corrosion resistance of high-hardness materials is higher than that of low-hardness materials, which is related to the precipitation and coarsening of tempered carbide. To reduce the hardness of materials, a higher temperature or longer time are needed during the tempering. As a result, there are more carbide precipitates with a larger size. The material in this research is the Cr-Mo-V alloy steel. After oil quenching at 1030 °C and tempering at high temperature, the structure is tempered martensite, while carbide dispersed.

SEM images of three hardness materials are shown in **Figures 11a**, **11c** and **11e**. Carbides are white and the main carbide types and shapes are divided into[35–38] irregular spherical $M_{23}(C, N)_6$, short rod/rod $M_7(C, N)_3$, short

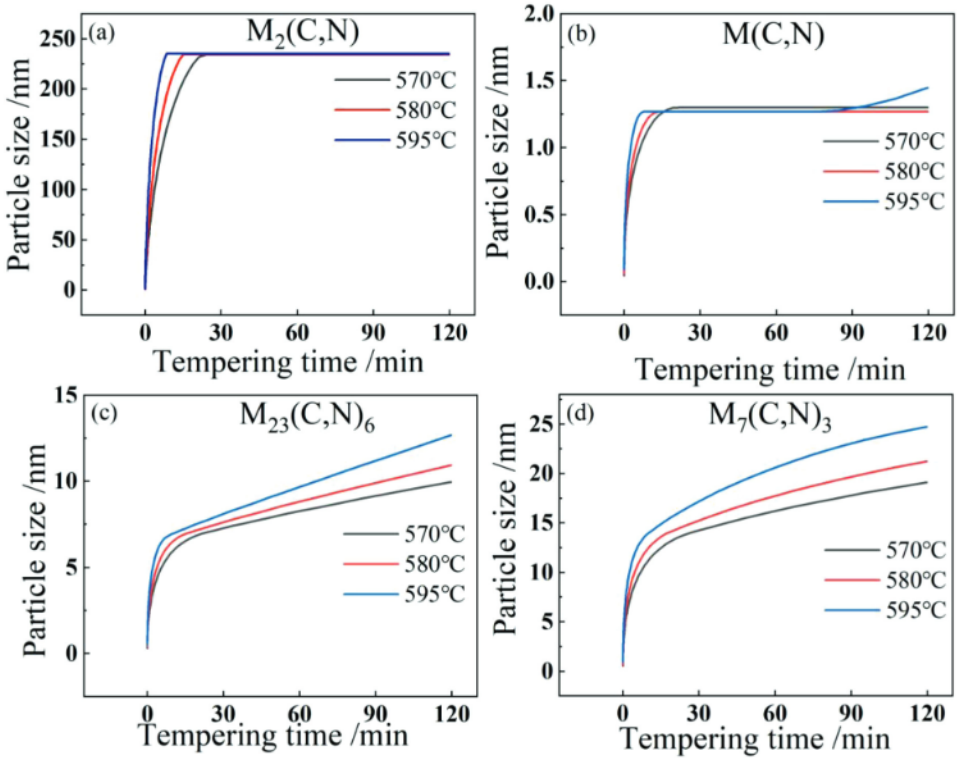

Figure 13: Calculation of the carbide-size change during tempering by JMatPro 7.0 software: a) $M_2(C, N)$, b) M(C, N), c) $M_{23}(C, N)_6$, d) $M_7(C, N)_3$

rod/rod $M_2(C, N)$ and small granular M(C, N). The enrichment of Cr mainly includes $M_{23}(C, N)_6$ and $M_7(C, N)_3$.[39] When observing carbides on **Figures 11a** to **11f**, we can see that with the increase in the tempering temperature, the hardness changed from high to low, the area gradually occupied by carbides increases, the size of carbides becomes larger, and the size of irregular spherical carbides enriched with Cr also becomes larger. By rendering the color of carbides, the carbides are represented in red, and the rest is black in order to use Image Pro Plus software analysis pictures and calculate the percentage of the carbides in the observed area. The statistical results are shown in **Figure 12**. It can be seen from **Figure 12** that the percentage of carbide area in field increases gradually with the decrease in the hardness, from 16.36 % to 24.32 %.

With the JMatPro software, the change in the main carbide size with the tempering time was simulated. As shown in **Figure 13**, the sizes of the main four types of carbides, $M_2(C, N)$ and M(C, N) carbides, changed little after tempering for 2 h. The sizes of $M_{23}(C, N)_6$ and $M_7(C, N)_3$ increased, and they increased more when the tempering temperature was high, while the proportion of the carbide area from **Figure 12** increased. It also confirms the increase in the carbide size, indicating that with the increase in the tempering temperature, the carbide coarsens. Compared with the other types of carbides, the $M_{23}(C, N)_6$ phase enriched by Cr is easily coarsened.[40,41] The coarsening of carbides leads to the consumption of Cr in the matrix, which reduces the corrosion resistance of the base metal.[22,23]

The polarization curve is critical for the evaluation of the corrosion-reaction characteristics from both the kinetic and thermodynamic point of view.[42] **Figure 14** shows potentiodynamic polarization curves for the three hardness types, including high-hardness, middle-hardness, and low-hardness specimens. Through the Tafel linear extrapolation method, we obtained the intersection point of anodic and cathodic polarization curves, representing the corrosion potential. We could find that it moves in the negative direction with the increasing hardness. Although the change in the corrosion potential is relatively small, the change in the current densities is large. Logarithmic current density corresponding to the corrosion potential, converted to the current density, marks the value in the figure. In conclusion, due to the polarization curves of dynamic potential, we know that the current density increases with decreased hardness, from 28.53 μA/mm² to 40.93 μA/mm². Therefore, high-hardness materials have better corrosion resistance than low-hardness materials.

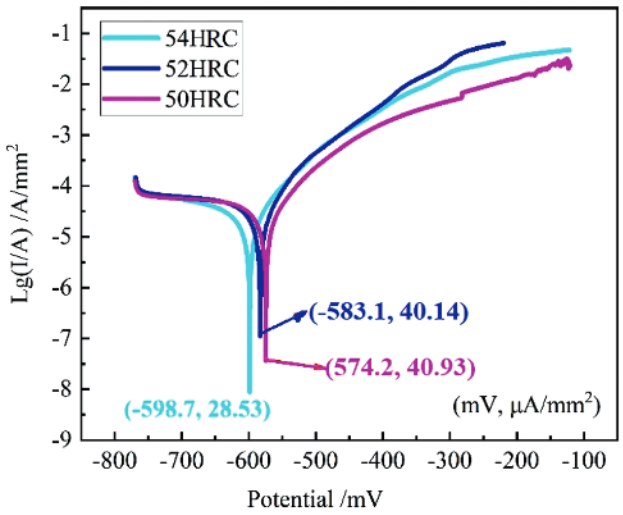

Figure 14: Potentiodynamic polarization curves for the three hardness materials

5 CONCLUSIONS

By studying the alternate immersion corrosion of SDCM steel for hot stamping, the following conclusions are obtained:

(1) No matter how hard the material is, when stress is applied, the corrosion mode is uniform and the stress promotes the corrosion rate. For low-hardness materials, the corrosion rate is always higher than that of medium- and high-hardness materials.

(2) Because of the presence of the corrosion removal layer (CRL), the maximum corrosion-pit depth is reduced. Therefore, it is not right to use the maximum corrosion-pit depth to assess the corrosion hazard, resulting in incorrect evaluation results. The degree of corrosion damage is accurately described using the CPD ρ_v remaining on the corrosion surface together with the maximum corrosion-pit depth. For the three kinds of hardness materials, the CPD ρ_v decreases with the increase in the stress, and the corrosion rate increases with the increase in the stress. This indicates that stress promotes corrosion and leads to an increase in the CRL and a decrease in the corrosion-pit size. From low to high hardness, both the CPD ρ_v and corrosion resistance increase gradually.

(3) The maximum corrosion-pit depth does not increase with the increase in the stress. For medium- and low-hardness materials, the maximum corrosion-pit depth and stress are in the form of an "S" curve. The maximum corrosion-pit depth of low-hardness materials is not sensitive to the stress. For medium-hardness materials, the maximum corrosion-pit depth increases significantly under a higher stress (about 700 MPa), reaching 227.12 μm. The maximum corrosion-pit depth and stress are exponential for the high-hardness material at 100 MPa. When the stress exceeds 100 MPa, the maximum corrosion-pit depth increases slowly with the increase in the stress, having a maximum corrosion value of 114.41 μm.

(4) The hardness of the alloy changes from high to low, the percentage of the carbide area in the field of view increases gradually, from 16.36 % to 24.32 %, and the irregular spherical carbide $M_{23}(C, N)_6$ rich in Cr is coarsened. Therefore, Cr is consumed by the material,

which leads to a decline in the corrosion resistance of the material. Through the polarization curve of dynamic potential, we know that the current density increases with decreased hardness from 28.53 μA/mm^2 to 40.93 μA/mm^2.

Acknowledgment

This work was financially supported by the National Key R&D Program of China under grant NO. 2016YFB00300400, and Guangdong Province Key Area R&D Program of China under grant NO. 2020B010184002.

The authors declare that there is no conflict of interest.

6 REFERENCES

[1] S. Li, The Study on microstructure and high temperature friction and wear mechanism of new type hot stamping die steel, Shanghai University, Shanghai 2017 (in Chinese)

[2] G. A. Zhang, Y. F. Cheng, On the fundamentals of electrochemical corrosion of X65 steel in CO2-containing formation water in the presence of acetic acid in petroleum production, Corrosion Science, 51 (**2009**) 1, 87–94, doi:10.1016/j.corsci.2008.10.013

[3] F. Caleyo, L. Alfonso, J. Alcantara, On the estimation of failure rates of multiple pipeline system, J. Press. Vessel Technol., 130 (**2006**) 2, 1030–1036, doi:10.1115/1.2894292

[4] G. Van Boven, W. Chen, R. Rogge, The role of residual stress in neutral pH stress corrosion cracking of pipeline steels. Part I: Pitting and cracking occurrence, Acta Mater., 55 (**2007**) 1, 29–42, doi:10.1016/j.actamat.2006.08.037

[5] J. Yu, H. Wang, Y. Yu, Corrosion behavior of X65 pipeline steel: Comparison of wet–dry cycle and full immersion, Corrosion Science, 133 (**2018**), 276–287, doi:10.1016/j.corsci.2018.01.007

[6] A. Turnbull, K. Mingard, J. D. Lord, Sensitivity of stress corrosion cracking of stainless steel to surface machining and grinding procedure, Corrosion Science, 53 (**2011**) 10, 3398–3415, doi:10.1016/j.corsci.2011.06.020

[7] M. Takano, H. Takaku, Stress Corrosion Cracking of Type 304 Stainless Steel under Residual Stress, Corrosion, 37 (**1981**) 3, 142–146, doi:10.5006/1.3622157

[8] C. Li, Y. Ma, Y. Li, F. Wang, EIS monitoring study of atmospheric corrosion under variable relative humidity, Corrosion Science, 52 (**2010**) 11, 3677–3686, doi:10.1016/j.corsci.2010.07.018

[9] T. Kamimura, S. Nasu, T. Segi, Corrosion behavior of steel under wet and dry cycles containing Cr^{3+} ion, Corrosion Science, 45 (**2003**), 1863–1879, doi:10.1016/S0010–938X(03)00023–4

[10] A. Nishikata, Y. Ichihara, Influence of electrolyte layer thickness and pH on the initial stage of the atmospheric corrosion of iron, Journal of the Electrochemical Society, 144 (**1997**) 4, 1244–1252, doi:10.1149/1.1837578

[11] E. M. Gutman, Mechanochemistry and Corrosion Protection of Metal, Science Press, Beijing 1989

[12] K. M. Kim, J. H. Park, H. S. Kim, Effect of plastic deformation on the corrosion resistance of ferritic stainless steel as a bipolar plate for polymer electrolyte membrane fuel cells, Int. J. Hydrogen Energy, 37 (**2012**) 10, 8459–8464, doi:10.1016/j.ijhydene.2012.02.127

[13] C. J. Lin, Z. D. Feng, F. L. Lin, Electrochemical behaviors of the loaded stainless steel in dilute thiosulphate solution, Journal of Electrochem., 4 (**1995**) 1, 439–445

[14] D. Chastell, P. Doig, P. Flewitt, K. Ryan, The influence of stress on the pitting susceptibility of 12%CrMoV martensitic stainless steel, Corrosion Science, 19 (**1979**) 5, 335–341

[15] L. Linghua, Study on stress corrosion cracking behavior in the welded rotor joint of nuclear steam turbine, East China University of Science and Technology, Shanghai 2017 (in Chinese)

[16] K. Tong, X. Sheng–qi, W. Xian–ping, Effect of high-frequency induction hardening on stress corrosion of a 12 % Cr martensitic stainless steel, 2nd Energy Materials Conference, San Diego, CA, Feb 26–Mar 02, 2017, doi:10.1007/978–3–319–52333–0_17

[17] A. Ning, W. Mao, X. Chen, Precipitation Behavior of Carbides in H13 Hot Work Die Steel and its Strengthening during Tempering, Metal Science and Heat Treatment, 52 (**2010**) 7–8, 393–395, doi:10.3390/met7030070

[18] L. Mu, Z. Xingfeng, H. Lizhan, Microstructural Evolution and Carbide Precipitation in a Heat-Treated H13 Hot Work Mold Steel, Metallography Microstructure and Analysis, 5 (**2016**) 6, 520–527, doi:10.1007/s13632–016–0318–5

[19] Y. Shu-Hung, C. Liu-Ho, P, Yeong-Tsuen, Relative Dimensional Change Evaluation of Vacuum Heat-Treated JIS SKD61 Hot-Work Tool Steels, Journal of Materials Engineering and Performance, 23 (**2014**) 6, 2075–2082, doi:10.1007/s11665–014–0961–4

[20] M. B. Kermani, J. C. Gonzales, C. Linne, M. Dougan, R. Cochrane, Development of Low Carbon Cr-Mo Steels with Exceptional Corrosion Resistance for Oilfield Applications, NACE International, 2001, Paper No. 01065

[21] P. I. Nice, H. Takabe, M. Ueda, The Development and Implementation of a New Alloyed Steel for Oil and Gas Production Wells, NACE International, 2000, Paper No. 154

[22] Z. Qingchun, W. Xiaochun, M. Na, Microstructure evolution and kinetic analysis of DM hot-work die steels during tempering, Materials Science and Engineering A, 528 (**2011**) 18, 5696–5700, doi:10.1016/j.msea.2011.04.024

[23] G. Jinbo, L. Jingyuan, Y. Jun, Microstructural evolution and mechanical property changes of a new nitrogen-alloyed Cr–Mo–V hot-working die steel during tempering, Materials Science and Engineering A, 804 (**2021**), 140721, doi:10.1016/j.msea.2020.140721

[24] S. W. Ooi, T. I. Ramjaun, C. Hulme-Smith, Designing steel to resist hydrogen embrittlement Part 2 – precipitate characterization, Mater. Sci. Technol., 34 (**2018**) 14, 1747–1758, doi:10.1080/02670836.2018.1496536

[25] C. E. Cerdan, S. W. Ooi, J. R. Guaurav, Effect of tempering heat treatment on the CO_2 corrosion resistance of quench-hardened Cr-Mo low-alloy steels for oil and gas applications, Corrosion Science, 154 (**2019**), 36–48, doi:10.1016/j.corsci.2019.03.036

[26] V. A. Alves, C. M. A. Brett, A. Cavaleiro, Influence of heat treatment on the corrosion of high speed steel, J. Appl. Electrochem., 31 (**2001**) 1, 65–72, doi:10.1023/A:1004157623466

[27] O. K. Duo, Y. C. Pu, A. Inceclk, Computation of ultimate strength of locally corroded unstiffened plates under uniaxial compression, Mar. Struct., 20 (**2007**) 1–2, 100–114, doi:10.1016/j.marstruc.2007.02.003

[28] A. Jarrah, M. Bigerelle, G. Guillemot, A generic statistical methodology to predict the maximum pit depth of a localized corrosion process, Corros. Sci., 83 (**2011**) 8, 2453–2467, doi:10.1016/j.corsci.2011.03.026

[29] A. Valor, F. Caleyo, D. Rivas, Stochastic approach to pitting-corrosion-extreme modelling in low-carbon steel, Corros. Sci., 52 (**2010**) 3, 910–915, doi:10.1016/j.corsci.2009.11.011

[30] L. H. Zhou, Study on microstructure and properties of SDCM hot stamping tool steels, Shanghai University, Shanghai 2015, 37–48 (in Chinese)

[31] GB/T 15970.2–2000, Corrosion of metals and alloys – Stress corrosion testing – Part 2: Preparation and use of bent-beam specimens (in Chinese)

[32] GB/T 19292.4–2018, Corrosion of metals and alloys – Corrosivity of atmospheres – Part 4: Determination of corrosion rate of standard specimens for the evaluation of corrosivity

[33] T. T. N. Lan, N. T. P. Thoa, R. Nishimura, Y. Tsujino, M. Yokoi, Y. Maedab, Atmospheric corrosion of carbon steel under field exposure

in the southern part of Vietnam, Corros, Sci., 48 (**2006**) 1, 179–192, doi:10.1016/j.corsci.2004.11.018

[34] M. Yhantai, L. Ying, W. Fuhui, The atmospheric corrosion kinetics of low carbon steel in a tropical marine environment, Corros. Sci., 52 (**2010**) 5, 1796–1800, doi:10.1016/j.corsci.2010.01.022

[35] Y. Liu, Z. Liu, C. Zhang, Calculation and analysis of valence electron structure of Mo_2C and V_4C_3 in hot working die steel, Journal of Iron and Steel Research International, 13 (**2006**) 5, 50–56, doi:10.1016/S1006–706X(06)60026–5

[36] S. W. Xia, P. Zuo, Y. Zeng, Influence of nickel on secondary hardening of a modified AISI H13 hot work die steel, Materialwissenschaft und Werkstofftechnik, 50 (**2019**) 2, 197–203, doi:10.1002/mawe.201700205

[37] A. Karaaslan, C. Akca, The influence of carbide distribution on the properties of hot work tool steels, 18th International Conference on Metallurgy and Materials, Hradec Nad Moravici, Czech Republic, May 19–21, 2009, 521–524

[38] Z. Yan, Research on microstructure evolution behaviour of die-casting die steel based on thermo-mechanical loading, Shanghai University, Shanghai 2019 (in Chinese)

[39] A. Ning, W. Mao, X. Chen, Precipitation behaviour of carbides in H13 hot work die steel and its strengthening during tempering, Metals, 7 (**2017**) 70, 2–15, doi:10.3390/met7030070

[40] X. B. Hu, L. Li, X. C. Wu, M. Zhang, Coarsening Behavior of M23C6 Carbides after Ageing or Thermal Fatigue in AISI H13 Steel with Niobium, International Journal of Fatigue, 28 (**2006**) 3, 175–182, doi:10.1016/j.ijfatigue.2005.06.042

[41] J. Wang, Z. Xu, X. Lu, Effect of the quenching and tempering temperatures on the microstructure and mechanical properties of H13 steel, Journal of Materials Engineering and Performance, 29 (**2020**) 3, 1849–1859, doi:10.1007/s11665–020–04686–0

[42] J. Xie, T. A. Alpas, D. O. Northwood, The effect of erosion on the electrochemical properties of AISI 1020 steel, Journal of Materials Engineering and Performance, 12 (**2003**) 1, 77–86, doi:10.1361/105994903770343510